The Astrophysical Journal Letters, 861:L15 (6pp), 2018 July 10 https://doi.org/10.3847/2041-8213/aacf98

In Situ Generation of Transverse Magnetohydrodynamic Waves from Colliding Flows in the Solar Corona

Patrick Antolin[1], Paolo Pagano[1], Ineke De Moortel[1], and Valery M. Nakariakov[2,3]
[1] School of Mathematics and Statistics, University of St Andrews, St Andrews, Fife KY16 9SS, UK; patrick.antolin@st-andrews.ac.uk
[2] Centre for Fusion, Space and Astrophysics, University of Warwick, Coventry CV4 7AL, UK
[3] School of Space Research, Kyung Hee University, Yongin, 446-701 Gyeonggi, Republic of Korea
Received 2018 April 18; revised 2018 June 25; accepted 2018 June 27; published 2018 July 9

Abstract

Transverse magnetohydrodynamic (MHD) waves permeate the solar atmosphere and are a candidate for coronal heating. However, the origin of these waves is still unclear. In this Letter, we analyze coordinated observations from *Hinode*/Solar Optical Telescope (SOT) and *Interface Region Imaging Spectrograph (IRIS)* of a prominence/coronal rain loop-like structure at the limb of the Sun. Cool and dense downflows and upflows are observed along the structure. A collision between a downward and an upward flow with an estimated energy flux of 10^7–10^8 erg cm^{-2} s^{-1} is observed to generate oscillatory transverse perturbations of the strands with an estimated $\approx$40 km s^{-1} total amplitude, and a short-lived brightening event with the plasma temperature increasing to at least 10^5 K. We interpret this response as sausage and kink transverse MHD waves based on 2D MHD simulations of plasma flow collision. The lengths, density, and velocity differences between the colliding clumps and the strength of the magnetic field are major parameters defining the response to the collision. The presence of asymmetry between the clumps (angle of impact surface and/or offset of flowing axis) is crucial for generating a kink mode. Using the observed values, we successfully reproduce the observed transverse perturbations and brightening, and show adiabatic heating to coronal temperatures. The numerical modeling indicates that the plasma β in this loop-like structure is confined between 0.09 and 0.36. These results suggest that such collisions from counter-streaming flows can be a source of in situ transverse MHD waves, and that for cool and dense prominence conditions such waves could have significant amplitudes.

Key words: magnetohydrodynamics (MHD) – Sun: activity – Sun: corona – Sun: filaments, prominences – Sun: oscillations – waves

Supporting material: animations

1. Introduction

Transverse magnetohydrodynamic (MHD) waves permeate the solar atmosphere and constitute a possible candidate for coronal heating (for a review, see for example Arregui et al. 2012; De Moortel & Nakariakov 2012; Arregui 2015). A main source of evidence of these waves comes from observations of prominences and coronal rain, in which the naturally cold, dense, and optically thicker plasma conditions allow much higher spatial resolution and reduced line-of-sight (LOS) confusion (Lin et al. 2005; Okamoto et al. 2007; Ning et al. 2009; Lin 2011; Hillier et al. 2013; Schmieder et al. 2013; Okamoto et al. 2015; Vial & Engvold 2015). However, the origin of these waves (in coronal and prominence structures) remains unclear and is usually assumed to be in convective motions, or through mode conversion of *p*-modes propagating from the solar interior.

Another commonly observed feature of cool coronal structures, such as prominences and rainy loops, are field-aligned flows with speeds of 10–100 km s^{-1} and 40–200 km s^{-1}, respectively (Ofman & Wang 2008; Antolin & Rouppe van der Voort 2012; Alexander et al. 2013; Kleint et al. 2014). Both downflows and upflows are observed along the legs of prominences (Vial & Engvold 2015). These longitudinal dynamics are commonly associated with the formation mechanism of prominences or coronal rain, such as thermal instability or thermal non-equilibrium (Antiochos et al. 1999; Karpen et al. 2001; Antolin et al. 2010; Xia et al. 2017).

Through coordinated observations of a prominence/coronal rain complex (Section 2) with *Hinode* (Kosugi et al. 2007), the *Interface Region Imaging Spectrograph* (*IRIS*; De Pontieu et al. 2014), and the *Solar Dynamics Observatory* (*SDO*; Pesnell et al. 2012), and numerical MHD modeling (Section 4), we show that in situ collisions from such counter-streaming flows could be a source of transverse MHD waves in the corona.

2. Observations

On 2014 April 3, *SDO*, *IRIS*, and *Hinode* co-observed a prominence/coronal rain complex on the West limb of the Sun (*IRIS–Hinode* operation plan 254), shown in Figure 1. The *Hinode* Solar Optical Telescope (SOT; Suematsu et al. 2008; Tsuneta et al. 2008) observed from 13:16 UT to 14:30 UT in the Ca II H line, with a cadence of 8 s (1.23 s exposure), with 0.″109 pixel^{-1} platescale, and a field-of-view (FOV) of 111″ × 111″, centered at helioprojective coordinates (x, y) = (996.5,31.1). *IRIS* observed from 13:16 UT to 14:53 UT with a four-step sparse raster program (OBS ID 3840259471), with a cadence for the Slit-Jaw Imager (SJI) of 18.27 s (exposure time of 8 s) and 9 s for the spectrograph SG (roughly 37 s per raster position), with 0.″166 pixel^{-1} platescale, a FOV of 127″ × 128″ centered at (x, y) = (1007.1,34.2), containing the SOT FOV. The *IRIS* observing program included both the SJI 2796 and SJI 1400 filtergrams, which are dominated by Mg II k emission at 2796.35 Å around 2 × 10^4 K and Si IV emission at 1402.77 Å around 10^5 K, respectively. The images from the Atmospheric Imaging Assembly (AIA;

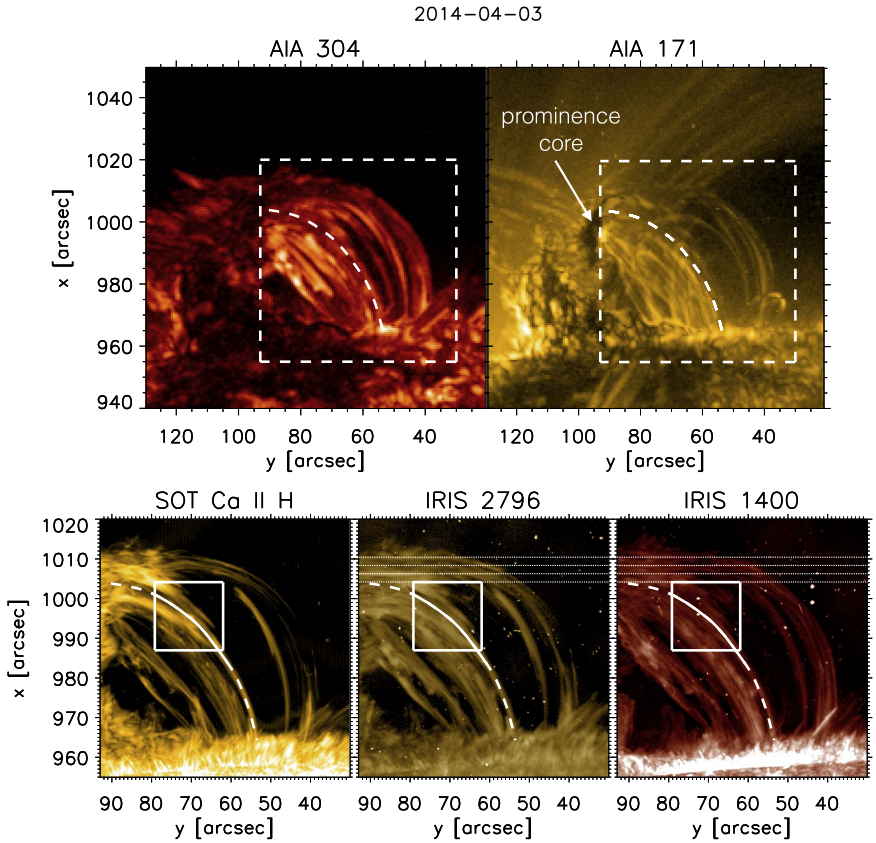

Figure 1. From top left to bottom right we show variance images (sum of squared differences from an 8-minute average image) in the AIA 304, AIA 171, in the SOT Ca II H, SJI 2796, and SJI 1400 of *IRIS*. The FOV of the bottom three panels is shown as a dashed square in the top two panels. A particular set of downflows is followed along one of these structures (white dashed/solid curve). The horizontal dotted lines in the *IRIS* panels indicate the location of the slit during the four-step raster. Note that the solar east–west direction corresponds to the vertical axes in the panels.

Lemen et al. 2012) were in level 1.5. Their cadence is 12 s, with a platescale of $0\farcs6$ pixel^{-1}.

The SOT data set was processed using the `FG_PREP` Solarsoft routine. The SJI data corresponds to level 2 data (De Pontieu et al. 2014), which includes correction for thermal variations of the pointing by co-aligning each image using a cross-correlation maximization routine. SOT, *IRIS,* and AIA data were co-aligned manually.

The target of the observations was a loop-like structure stemming from a high-prominence ($\approx 55''$ above the limb) core, reminiscent of the model by Keppens & Xia (2014). In Figure 1 we show a variance image of this structure in Ca II H, SJI 2796, and SJI 1400, where the variance is taken over within the first 8 minutes of the observation.

3. Colliding Flows

The focus of the present investigation is the main loop-like structure connected to the prominence core seen in the middle of the images in Figure 1. The flows along this loop structure are clumpy and multi-stranded, particularly in the higher-resolution Ca II H intensity images, a general characteristic of coronal rain material when observed at high resolution (Antolin et al. 2015). Mostly downflows are observed, stemming from the prominence core (top left) toward the surface. Additionally, and in contrast to the usual coronal rain, the current case also exhibits a significant amount of upflows probably caused by dips at the loop apex, enhancing thermal instability.

We follow a particular set of clumps during their downward trajectory (dashed curve in Figures 1 and 2) at a constant velocity of ≈ 50 km s^{-1} in the plane-of-the-sky (POS). At high resolution in Ca II H, the clumps are $0\farcs3$–$1\farcs4$ in width (across the loop), with a continuously variable length of a few arcsec. Halfway along the loop at $t = 13.23$ UT the clumps' intensities in all three channels suddenly increase, and a bright front of about $2''$ in width is observed (visible in Figure 2). Afterward, the downward speeds of some of the clumps are reduced by half, as seen in the time–distance diagram along the loop (the three bottom-left panels in Figure 2). In addition, the clumps are seen to oscillate transversely in Ca II H following the intensity increase. This is best seen in the time–distance diagram transverse to the loop (bottom-right panel in Figure 2), where we follow the clump along its downward trajectory. We can see that some clumps undergo an outward transverse motion of $\approx 1''$ (radially away from the Sun, positive transverse distance in the panel), while others undergo an inwards transverse motion of similar amplitude. The initial transverse velocity in the POS is ≈ 25 km s^{-1}. The outward transverse motion can be tracked for longer times and the oscillation is damped in two–three periods. Note that the period of the oscillation increases from the first to the second oscillation, from 50–60 s to 80–90 s.

The *IRIS* SJIs reveal an upward flow with a speed of ≈ 40 km s^{-1} that seems to collide with the downward flow (see the time–distance diagram along the loop). The time of collision coincides with both the brightness increase in all three channels and the start of the transverse oscillation. This

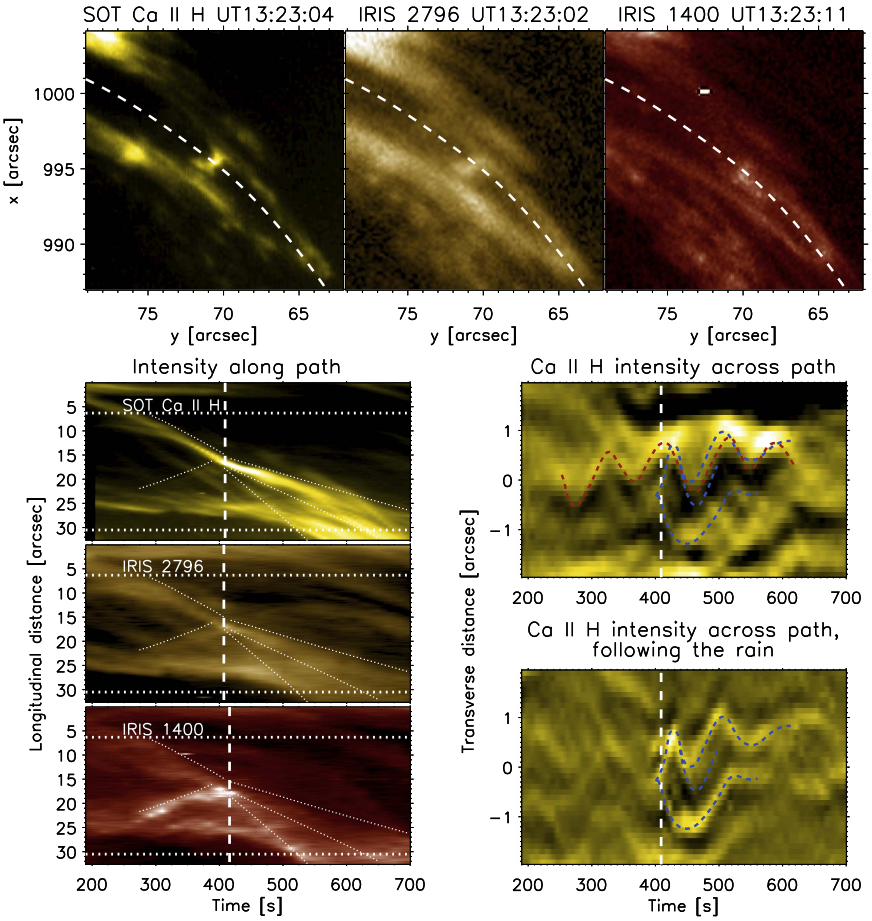

Figure 2. The three top panels show, from left to right, the region indicated by the small white square (solid lines) of Figure 1, in the Ca II H line of SOT, the SJI 2796, and SJI 1400 of *IRIS*. The white dashed curve shows the path of counter-streaming plasma clumps. The time–distance diagram along this path is shown in the three left panels, where distance is measured from the top of the path shown in Figure 1. The intensity is integrated over a width of 1″. The horizontal dotted lines in these panels indicate the top and bottom coordinates along the trajectory within the FOV of the top three panels. The vertical dashed line indicates the closest time to collision for each channel. The middle and bottom-right panels show transverse cuts to the trajectory of the clumps. The contours of the brightest oscillatory paths are traced visually in dashed red and blue curves, respectively, for the middle and bottom-right panels. In the middle panel the intensity along part of the path (solid curve in Figure 1) is integrated for each transverse cut. In the lower panel the downflowing set of clumps is followed, and at each time the transverse cut to the trajectory is plotted. An animation starting around 13:16:15 UT and ending at 13:28:15 UT and a duration of 15 s is available.

(An animation of this figure is available.)

upward flow is clearly visible in SJI 1400, but barely visible in SJI 2796 and Ca II H. This intensity difference across the channels suggests that the upward flow is about 10 times hotter, with a temperature around 10^5 K. This event suggests that a collision occurs between the downward and upward flows, which then leads to the generation of transverse MHD waves.

The middle-right panel in Figure 2 shows the presence of transverse MHD waves along the loop even prior to the flow collision, with a period of ≈90–100 s. The oscillation initiated by the collision (blue curves in the panels) is different from this background oscillation (red curves). For instance, the time of the flow collision ($t \approx 410$ s) and the subsequent maxima is initially out-of-phase with this background oscillation. The increasing period of the generated transverse oscillation leads to an in-phase second maxima.

We have estimated the total densities of the plasma toward the prominence core with the help of the AIA data. These estimates are based on extreme ultraviolet (EUV) absorption by the cool material (mainly neutral hydrogen and helium) in the AIA wavelengths following the technique by Landi & Reale (2013) and Antolin et al. (2015). Taking a 5% helium abundance, we find values between 6×10^{10} and 3×10^{11} cm^{-3}, in agreement with previous measurements in prominences (Vial & Engvold 2015) and coronal rain (Antolin et al. 2015).

Due to its position and orientation, the *IRIS* slit captures a significant fraction of the loop near its apex (see Figure 1). Hence, the slit captures the spectra of several flows directed along the loop. These flows produce positive/negative slopes for upward/downward flows, respectively, in the time–distance diagram along the slit (see Figure 3). For each wavelength position (corresponding to a Doppler velocity $v_{\rm Dopp,obs}$, assuming the wavelength value from CHIANTI for the zero velocity; Dere et al. 2009) we select the most distinct paths and measure the slopes, which corresponds to the POS velocity along the slit $v_{\rm POS}$. These measurements are shown in the scatter plot of the bottom panel. The quantities follow the relation $v_{\rm Dopp,obs} = v_{\rm POS}\tan(\theta) + v_\alpha$, where v_α corresponds to the zero Doppler velocity in the reference frame of the loop, and θ corresponds to the angle of the flow path (at the loop apex) with the POS plane. We find $\theta = 49.5° \pm 1.2°$ and $v_\alpha = 20.2 \pm 1.6$ km s^{-1}. This implies that the total velocity of a flow with POS velocity of 50 km s^{-1} is close to 77 km s^{-1}, and that the transverse amplitude of the wave is ≈40 km s^{-1}.

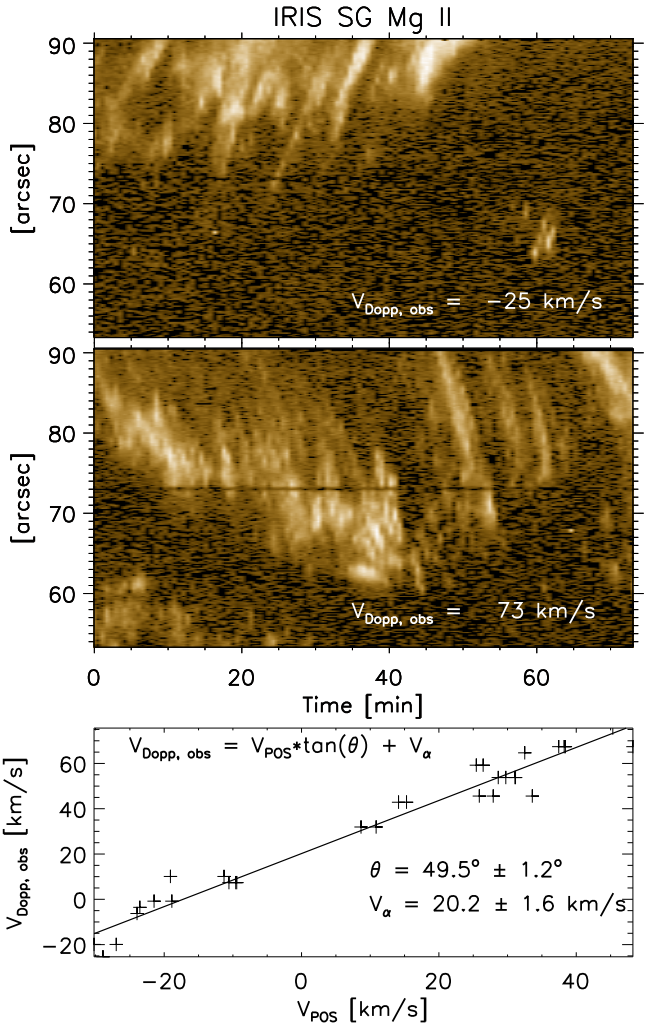

Figure 3. The top two panels show the time–distance diagram along part of the bottom-most slit position (tangent to the loop apex) at two wavelength positions. The slopes (v_{POS}) of several paths of clumps are measured for each wavelength position ($v_{Dopp,obs}$) and plotted in the bottom panel. Positive/negative slopes correspond, respectively, to negative/positive V_{POS}.

4. MHD Model

In order to interpret our observations, we set up a 2D MHD model of counter-streaming plasma clumps.

We consider a 2D spatial domain that extends for 12 Mm in the x-direction (field aligned) and 6 Mm in the y-direction. The magnetic field, B_0, is uniform and directed along the x-direction. Two trapezoidal clumps are placed at a distance of 4 Mm and are 1 Mm wide and 3 Mm long in a background corona where the density is $n_0 = 1.2 \times 10^9\,\mathrm{cm}^{-3}$ and the temperature is $T_0 = 1$ MK. The clumps are n_c times denser than the background plasma and colder in order to maintain pressure equilibrium. The plasma within the clumps has an initial velocity of $V_B = \pm 70\,\mathrm{km\,s}^{-1}$. The shape of the clumps is such that the two facing sides are inclined in the same direction with an angle $\phi = 50°$. We numerically solve the set of ideal MHD equations using the MPI-AMRVAC software (Porth et al. 2014). We neglect non-ideal effects, as they would act on timescales longer than the observed evolution.

The observations suggest lower and upper limits for the density contrast of the clumps. Therefore, we model a strong collision scenario where we have $n_c = 100$, and a weak collision scenario where we have $n_c = 25$. For each scenario we first run four simulations with different values of plasma β (0.02, 0.05, 0.2, 0.5) that defines a posteriori the field strength B_0. Figure 4(a) illustrates the density and magnetic field lines in the initial condition for all simulations.

The clumps move toward one another, leading to the compression of plasma between the clumps, which is adiabatically heated up to ∼3 MK and cools down to 750,000 K in ∼10 s due to mixing with the cold clump plasma. The pressure equilibrium no longer holds and the plasma expands in the y-direction, leading to the distortion of the magnetic field. Because of the inclination of the facing sides of the clumps, the magnetic field is distorted at two different locations with an offset along the x-direction. This geometry leads to the kink of the magnetic field, as shown in Figure 4(b). The magnetic field lines threading the clumps all appear similarly distorted. After the initial kink of the magnetic field, the kink propagates along the clumps at the kink speed, which increases once the wave leaves the clumps. We measure the kink amplitude as the difference between the maximum and minimum y-coordinates of the magnetic field line crossing the origin at $t = 0$ (blue lines in Figure 4(b)).

As the kink is generated by the imbalanced thermal pressure due to the compression between the clumps, the amplitude of the kink depends on the background plasma β. For the strong and weak collision scenarios, we derive the kink amplitude as a function of β and then, with a linear interpolation, we derive the best β value to match the observed kink amplitude. We find that the kink amplitude increases until a maximum is reached and then reduces (Figure 5(a)). As expected, the strong collision scenario leads to larger kink amplitudes and the higher the plasma β, the more the magnetic field is distorted. It is also evident that the wave period is longer for the larger plasma β that implies the decrease in the Alfvén speed.

Figure 5(b) shows the maximum kink amplitude for the two scenarios as a function of β. By means of this parameter space investigation, we derive that in the strong and weak collision scenarios the observed kink amplitude is matched when $\beta = 0.09$ and when $\beta = 0.36$, respectively. Therefore, by applying this simple model to the observed event we can constrain the value of the loop plasma β. While the initial distortion of the magnetic field is similar to a kink mode, once this travels away from the clumps the amplitude of the remaining perturbation decreases and becomes more similar to a sausage mode (symmetric oscillation around $y = 0$ axis). In particular for the strong collision scenario, this occurs between $\beta = 0.05$ and $\beta = 0.2$. For lower β, the collision is not strong enough to produce any significant long-lasting oscillation and for higher β, the post-collision magnetic field becomes so entangled that it no longer behaves as a wave guide. In the weak collision scenario we do not notice a visible persistence of sausage modes after the collision. Similarly, as long as the clumps' collision is ongoing, the continued compression keeps the magnetic field kinked, but the magnetic field distortion location drifts toward the external part of the clumps. Only after the collision process is over can the kink mode properly oscillate. Therefore, the wavelength of the initial kink oscillation depends on the length and speed of the clumps, as well as the plasma β.

To investigate the dependence on the shape of the clumps, we perform two more simulations (with the best β values for both scenarios) where the two clumps are symmetric and have

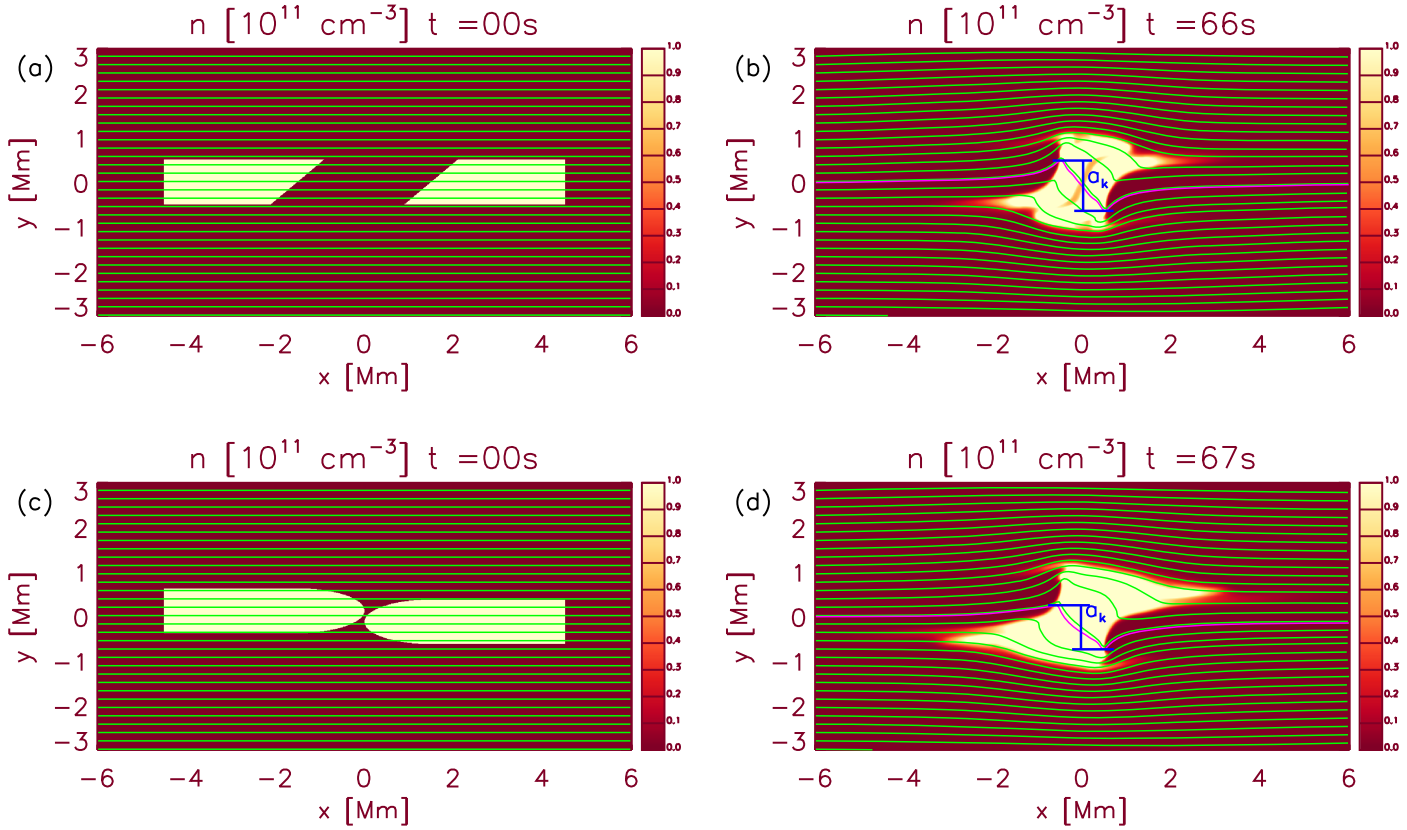

Figure 4. Maps of number density with overlaid magnetic field lines for the initial conditions of the simulations with trapezoidal or circular front clumps ((a) and (c)) and the times when the kink is maximum ((b) and (d)), for the strong collision scenario when $\beta = 0.098$. The blue lines mark the amplitude a_k of the kink. An animation starting at $t = 0$ s and ending at $t = 300$ s with a duration of 10 s is available.

(An animation of this figure is available.)

elliptic facing surfaces (Figure 4(c)). Here, the central axes of the clumps are offset, overlapping for 75% of their width. In this configuration, the asymmetry that induces the kink is given by this offset. The kink amplitude (Figure 4(d)) is found to be only $\sim$10% smaller than in the simulation with trapezoidal clumps. Hence, although the presence of an asymmetry is crucial to produce a kink-like perturbation, the exact nature of this asymmetry (shape of interface or offset) appears unimportant in the current framework. We intend to pursue a more complete parameter space investigation to identify more exactly the role and nature of this asymmetry. Future 3D simulations will address more properties of this mechanism for the generation of kink and sausage waves, including the generation of torsional waves.

5. Discussion and Conclusions

We have analyzed coordinated observations with *Hinode* and *IRIS* of flows along a loop-like structure connecting a prominence with the solar surface. A collision between a downflow and an upflow is observed at estimated total speeds of 80 km s^{-1} and 60 km s^{-1}, respectively (including Doppler and POS speeds). The densities of the flows are estimated to be around 6×10^{10}–3×10^{11} cm^{-3}. The flows are seen in SJI 2796 and 1400, indicating temperatures of 10^4–10^5 K. At high resolution with SOT in the Ca II H line the flows appear clumpy, with widths of 0.″3–1.″4. Coinciding with the time and location of collision, a bright and short-lived front is generated, indicating at least a 10-fold temperature increase. Also, at high resolution with SOT, these clumps are observed to oscillate transversely just after the collision, with an estimated total amplitude of $\approx$40 km s^{-1}. We estimate a combined kinetic and enthalpy energy flux for these flows of 10^7–10^8 erg cm^{-2} s^{-1}.

Through 2D MHD numerical modeling, we have reproduced the collision between two counter-streaming flows with conditions similar to those observed. Because the clump densities are the least well-defined parameter, we allow a range of 25–100 density contrast. Through a parameter space investigation, in order to reproduce the observed amplitude we find that the plasma β must be confined between 0.09 and 0.36, which correspond, respectively, to magnetic field values of 6.5 G and 3.4 G.

The modeling indicates that the presence of asymmetry between the colliding clumps leads to the in situ generation of trapped and leaky MHD waves, in particular transverse and sausage, which agrees with the initially out-of-phase (radial) oscillation of strands (characteristic of the sausage mode), followed by an in-phase transverse oscillation (characteristic of the kink mode). The observed increase in period is also well explained by the modeling: the wavelength of the transverse wave is set by the length of the clumps, which increases from the time of maximum compression. Transverse MHD waves may therefore be generated in situ in the corona through flow collision. For cool and dense prominence conditions, such waves could have significant amplitudes.

The temperature at the collision can increase to coronal values, explaining the sudden intensity increase in all three channels. No localized signature was found in the *SDO*/AIA channels (excluding AIA 304), possibly due to the increased

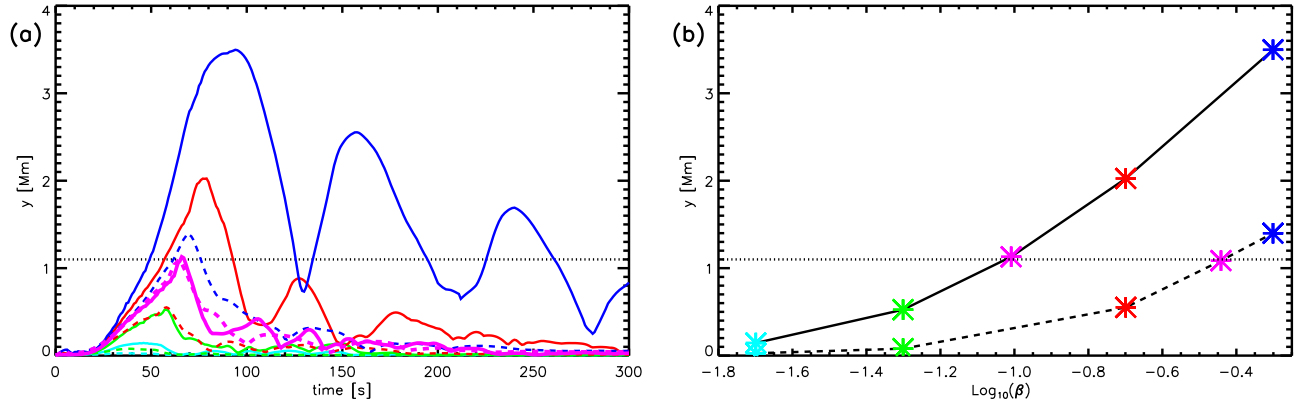

Figure 5. (a) Graph of the kink amplitude as a function of time for simulations with trapezoidal clumps. Solid and dashed lines correspond, respectively, to the strong and weak case scenario. (b) Maximum kink amplitude in each simulation as function of $\mathrm{Log}_{10}(\beta)$. Different colors mark the β value: light blue, green, red, and blue for $\beta = 0.02$, 0.05, 0.2, and 0.5, respectively. Magenta for the β values that match best the observed kink amplitude in both scenarios.

LOS integration or long ionization times. Nonetheless, similar signatures of counter-streaming flows and transverse MHD waves are observed at other times in this structure. The cumulative effect of such flow collisions (possibly explaining the observed background oscillation) and in situ generated transverse MHD waves (particularly the compressive waves) may contribute to the energy balance, which may explain the EUV emission of the entire structure.

This research has received funding from the UK Science and Technology Facilities Council (Consolidated Grant ST/K000950/1) and the European Union Horizon 2020 Research and Innovation Programme (grant agreement No. 647214). V.M.N. acknowledges the support of the BK21 plus program through the National Research Foundation funded by the Ministry of Education of Korea. *Hinode* is a Japanese mission developed and launched by ISAS/JAXA, with NAOJ as domestic partner and NASA and STFC (UK) as international partners. It is operated by these agencies in co-operation with ESA and NSC (Norway). *IRIS* is a NASA small explorer mission developed and operated by LMSAL with mission operations executed at NASA Ames Research Center and major contributions to downlink communications funded by ESA and the Norwegian Space Centre. This work used the DiRAC Data Centric system at Durham University, operated by the Institute for Computational Cosmology on behalf of the STFC DiRAC HPC Facility. This equipment was funded by a BIS National E-infrastructure capital grant ST/K00042X/1, STFC capital grant ST/K00087X/1, DiRAC Operations grant ST/K003267/1, and Durham University. DiRAC is part of the National E-Infrastructure. We acknowledge the use of the open source (gitorious.org/amrvac) MPI-AMRVAC software.

ORCID iDs

Patrick Antolin https://orcid.org/0000-0003-1529-4681
Paolo Pagano https://orcid.org/0000-0001-5274-515X
Ineke De Moortel https://orcid.org/0000-0002-1452-9330
Valery M. Nakariakov https://orcid.org/0000-0001-6423-8286

References

Alexander, C. E., Walsh, R. W., Régnier, S., et al. 2013, ApJL, 775, L32
Antiochos, S. K., MacNeice, P. J., Spicer, D. S., & Klimchuk, J. A. 1999, ApJ, 512, 985
Antolin, P., & Rouppe van der Voort, L. 2012, ApJ, 745, 152
Antolin, P., Shibata, K., & Vissers, G. 2010, ApJ, 716, 154
Antolin, P., Vissers, G., Pereira, T. M. D., Rouppe van der Voort, L., & Scullion, E. 2015, ApJ, 806, 81
Arregui, I. 2015, RSPTA, 373, 20140261
Arregui, I., Oliver, R., & Ballester, J. L. 2012, LRSP, 9, 2
De Moortel, I., & Nakariakov, V. M. 2012, RSPTA, 370, 3193
De Pontieu, B., Title, A. M., Lemen, J. R., et al. 2014, SoPh, 289, 2733
Dere, K. P., Landi, E., Young, P. R., et al. 2009, A&A, 498, 915
Hillier, A., Morton, R. J., & Erdélyi, R. 2013, ApJL, 779, L16
Karpen, J. T., Antiochos, S. K., Hohensee, M., Klimchuk, J. A., & MacNeice, P. J. 2001, ApJL, 553, L85
Keppens, R., & Xia, C. 2014, ApJ, 789, 22
Kleint, L., Antolin, P., Tian, H., et al. 2014, ApJL, 789, L42
Kosugi, T., Matsuzaki, K., Sakao, T., et al. 2007, SoPh, 243, 3
Landi, E., & Reale, F. 2013, ApJ, 772, 71
Lemen, J. R., Title, A. M., Akin, D. J., et al. 2012, SoPh, 275, 17
Lin, Y. 2011, SSRv, 158, 237
Lin, Y., Engvold, O., Rouppe van der Voort, L., Wiik, J. E., & Berger, T. E. 2005, SoPh, 226, 239
Ning, Z., Cao, W., Okamoto, T. J., Ichimoto, K., & Qu, Z. Q. 2009, A&A, 499, 595
Ofman, L., & Wang, T. J. 2008, A&A, 482, L9
Okamoto, T. J., Antolin, P., De Pontieu, B., et al. 2015, ApJ, 809, 71
Okamoto, T. J., Tsuneta, S., Berger, T. E., et al. 2007, Sci, 318, 1577
Pesnell, W. D., Thompson, B. J., & Chamberlin, P. C. 2012, SoPh, 275, 3
Porth, O., Xia, C., Hendrix, T., Moschou, S. P., & Keppens, R. 2014, ApJS, 214, 4
Schmieder, B., Kucera, T. A., Knizhnik, K., et al. 2013, ApJ, 777, 108
Suematsu, Y., Tsuneta, S., Ichimoto, K., et al. 2008, SoPh, 249, 197
Tsuneta, S., Ichimoto, K., Katsukawa, Y., et al. 2008, SoPh, 249, 167
Vial, J.-C., & Engvold, O. 2015, Solar Prominences (Dordrecht: Springer)
Xia, C., Keppens, R., & Fang, X. 2017, A&A, 603, A42